

THE *FERMI* GAMMA-RAY HAZE FROM
DARK MATTER ANNIHILATIONS AND ANISOTROPIC DIFFUSIONGREGORY DOBLER^{1,5}, ILIAS CHOLIS^{2,3,6}, & NEAL WEINER^{3,4,7}*Draft version January 13, 2013*

ABSTRACT

Recent full-sky maps of the Galaxy from the *Fermi Gamma-Ray Space Telescope* have revealed a diffuse component of emission towards the Galactic center and extending up to roughly ± 50 degrees in latitude. This *Fermi* “haze” is the inverse Compton emission generated by the same electrons which generate the microwave synchrotron haze at WMAP wavelengths. The gamma-ray haze has two distinct characteristics: the spectrum is significantly harder than emission elsewhere in the Galaxy and the morphology is elongated in latitude with respect to longitude with an axis ratio ≈ 2 . If these electrons are generated through annihilations of dark matter particles in the Galactic halo, this morphology is difficult to realize with a standard spherical halo and isotropic cosmic-ray diffusion. However, we show that anisotropic diffusion along ordered magnetic field lines towards the center of the Galaxy coupled with a prolate dark matter halo can easily yield the required morphology without making unrealistic assumptions about diffusion parameters. Furthermore, a Sommerfeld enhancement to the self annihilation cross-section of ~ 30 yields a good fit to the morphology, amplitude, and spectrum of both the gamma-ray and microwave haze. The model is also consistent with local cosmic-ray measurements as well as CMB constraints.

Subject headings:

1. INTRODUCTION

With the first year data release, the *Fermi Gamma-Ray Space Telescope* provided a wealth of new insights and detail of the gamma-ray sky. The energy range and angular resolution of the Large Area Telescope (LAT) on board *Fermi* has significantly advanced the understanding of many areas of gamma-ray astronomy, from point source studies like pulsars (Abdo et al. 2009a, 2010e; Saz Parkinson et al. 2010) and blazars (Abdo et al. 2009b, 2010d,f,b), to diffuse emissions from the extragalactic gamma-ray background (Abdo et al. 2010c; Ackermann et al. 2010b; Abdo et al. 2010a) and the interstellar medium (ISM) (Abdo et al. 2009c; Porter et al. 2009; Strong et al. 2010).

Recently, Dobler et al. (2010) assembled full-sky maps of the Galaxy using the published raw photon data from *Fermi* from several hundred MeV up to several hundred GeV. These maps of gamma-ray emission from the diffuse ISM are produced primarily through three processes: cosmic-ray (CR) protons collide with the ISM producing π^0 particles that decay to gammas, bremsstrahlung from CR electrons (and positrons) colliding with ions, and inverse Compton (IC) scattering of starlight, infrared, and CMB photons by CR electrons. Because bremsstrahlung and π^0 emission are due to collisions of CRs with the ISM, these emissions are highly spatially correlated with

other maps of the interstellar medium like the dust column density map of Schlegel et al. (1998). Since the IC emission is generated by interactions of CR electrons with the interstellar radiation field (ISRF) there is not a good morphological tracer of this emission at other energies. However, CR electrons are primarily accelerated in supernova (SN) remnants and so their injection morphology should be very disk-like. Although diffusion effects are important, for isotropic diffusion through the Galaxy the resultant IC emission should also be very disk-like.

Using template fitting techniques to morphologically regress out the emission from π^0 ’s, bremsstrahlung, and IC from disk electrons from the *Fermi* maps, Dobler et al. (2010) found an excess “haze” of IC emission towards the Galactic center (GC) extending ± 50 degrees in latitude and with an axis ratio of roughly 2.0. This *Fermi* haze is the gamma-ray counterpart to the microwave haze observed by the *Wilkinson Microwave Anisotropy Probe* (WMAP) as described in Finkbeiner (2004a) and Dobler & Finkbeiner (2008a). At WMAP wavelengths, the same electrons which generate the *Fermi* IC haze interact with the Galactic magnetic field to produce synchrotron microwaves. Recently Su et al. (2010) reconsidered the morphology, arguing for a “bubble”-like structure. Nonetheless, for reasons outlined in §2 we use the “haze” moniker throughout this paper, although we are considering effectively the same gamma-ray signal.

In both the gamma-ray and synchrotron cases, the haze emission is significantly harder than elsewhere in the Galaxy, implying that the electrons which produce the haze have a harder spectrum than the electrons accelerated and diffused through the Galactic disk. In fact, the required electron spectrum (number density per unit energy) is roughly $dN/dE \propto E^{-1}$ at high energies which is significantly harder than electrons generated by SN shock acceleration after taking into account diffusion ef-

¹ Kavli Institute for Theoretical Physics, University of California, Santa Barbara Kohn Hall, Santa Barbara, CA 93106 USA

² Astrophysics Sector, La Scuola Internazionale Superiore di Studi Avanzati and Istituto Nazionale di Fisica Nucleare, Sezione di Trieste, via Bonomea 265, 34136 Trieste, Italy

³ Center for Cosmology and Particle Physics, Department of Physics, New York University, New York, NY 10003 USA

⁴ School of Natural Sciences, Institute for Advanced Study, Princeton, NJ 08540

⁵ dobler@kitp.ucsb.edu

⁶ ilias.cholis@sissa.it

⁷ neal.weiner@nyu.edu

fects. In that case, the steady state spectrum is closer to $dN/dE \propto E^{-3}$.

The identification of the haze in both the WMAP and *Fermi* data imply that the haze is both real and that the underlying electron spectrum is very hard. It is this hard spectrum and the diffuse elongated morphology that are the defining characteristics of the emission, and any proposed origin for the electrons must match both of these features. For example, several authors have studied the connection between the haze electrons and young and middle aged pulsars (Zhang et al. 2009; Faucher-Giguere & Loeb 2010; McQuinn & Zaldarriaga 2010). The morphology however of the diffused electrons accelerated in pulsar winds would also be very disk-like and would not match the morphology⁸. Others have tried to reproduce the haze emission with a combination of increased SN rate and modified diffusion parameters (McQuinn & Zaldarriaga 2010; Gebauer & de Boer 2009), but this also cannot produce the observed morphology or the observed spectrum, even including possible reacceleration effects. Lastly, there has been speculation that both the gamma-ray haze (Linden & Profumo 2010) and the microwave haze (Mertsch & Sarkar 2010) are due to imperfect template subtraction, however neither of these criticisms has been able to produce the morphology or the spectrum (amplitude and shape) of the observations using simulations. Furthermore, the gamma-ray haze is visible in the *Fermi* sky maps *without performing any template fitting* demonstrating that it is clearly a real structure.

This work builds upon previous studies of the haze which explore the possibility that the haze electrons are generated through dark matter (DM) annihilations in the Galactic halo. Finkbeiner (2004b) originally showed that the microwave haze morphology and spectrum in the WMAP 1-year data was reasonably well matched by a DM model with a particle mass of $M_\chi \sim 100$ GeV and with a self annihilation cross-section $\langle\sigma v\rangle \sim 3 \times 10^{-26}$ cm³/s which is roughly that required to yield the observed relic density of DM $\Omega_{DM} \approx 0.23$ if the DM particle is a thermal relic of the Big Bang.

However, initial data from *Fermi* of the inner Galaxy suggested that the IC emission from the haze electrons extended up to at least ~ 200 GeV implying a DM particle mass of closer to ~ 1 TeV. Since the annihilation rate is proportional to the number density squared, this requires a $\langle\sigma v\rangle$ roughly 100 times the thermal relic value in order to match the data. With light force carriers, a “boost factor” of 100 in the Galactic halo is easily obtainable (Arkani-Hamed et al. 2009; Pospelov & Ritz 2009) via the Sommerfeld mechanism (Sommerfeld 1931; Hisano et al. 2005, 2004; Cirelli et al. 2008; Lattanzi & Silk 2009), in which $\langle\sigma v\rangle$ increases with decreasing relative velocity up to some saturation value, while still producing the correct relic density (Feng et al. 2010; Finkbeiner et al. 2010). Such a particle model is also consistent with local electron and positron CR anomalies observed by the *Payload for Antimatter Exploration and Light-nuclei Astrophysics* (PAMELA; Picozza et al. 2007; Adriani et al. 2009, 2010) satellite

and *Fermi* (Abdo et al. 2009d; Ackermann et al. 2010a) as shown by Cholis et al. (2009a) and Cholis & Weiner (2009). A model independent fit to all of the data (gammas, microwaves, and CRs) by Lin et al. (2010) confirms that the injection spectrum must be $E^2 dN/dE \propto E^2$ which is broadly consistent with the spectrum of a Sommerfeld enhanced DM annihilation scenario in which the main products are leptons.

These works have shown that the amplitude and spectrum of the haze are easily reproduced with a DM particle annihilation model; but here we are concerned primarily with the morphology. The morphology of the gamma-ray haze is the most difficult aspect to model since the haze is significantly elongated in latitude with respect to longitude. In fact, the geometry is impossible to realize with disk-like (or, as we show in §4, spherical) injection, ruling out SNe or pulsars as a possible source.

Such a geometry is also inconsistent with a spherical DM halo and isotropic diffusion. However, it is very likely that neither of these assumptions is accurate. Generically, DM N-body simulations of Milky Way sized halos imply prolate halos with an axis ratio of roughly 2 (Diemand et al. 2008; Kuhlen et al. 2008; Springel et al. 2008) and observations of the spatial distribution of Milky Way satellites imply a prolate halo oriented perpendicular to the Galactic disk (e.g., Zentner et al. 2005). In addition, the presence of any ordered magnetic field lines towards the GC implies that the electrons will not diffuse isotropically as they follow the fields. In §2 we discuss the morphology of the haze in more detail, and in §3 we outline our anisotropic diffusion model which produces a DM IC halo that closely resembles the observed morphology. In §4, we compare our model to the data (both the morphology, amplitude, and spectrum of the haze emission) and in §5 we summarize our conclusions.

2. HAZE MORPHOLOGY

Prior to the release of the gamma-ray data, the microwave haze was described by Finkbeiner (2004a) and Dobler & Finkbeiner (2008a) as being centered on the GC, roughly spherical, and decreasing in amplitude approximately as $1/r$ where r is the angular distance to the GC. However, such a microwave signal is limited by the extent of the B-field off the disk. The *Fermi* data on the other hand clearly show that the haze is in fact elongated in latitude b and extends to $|b| \sim 50$ degrees. Despite the lower angular resolution and signal-to-noise, the gamma-ray data give a more complete picture of the location of the haze electrons. The reason for the different morphologies is that the synchrotron amplitude is proportional to the magnetic field strength while the IC is proportional to the ISRF. Since the magnetic field falls off quickly with distance above the Galactic disk while the CMB amplitude is latitude independent, the microwave haze is confined to lower latitudes compared to the gamma-ray haze.

The detailed morphology of the gamma-ray haze close to the Galactic plane is difficult to determine. In Dobler et al. (2010), three methods of template fitting were used: 1) the actual *Fermi* data from 1.0-2.0 GeV was used as a full-sky template, 2) the Schlegel et al. (1998) (SFD) dust map was used alone, and 3) the SFD dust map, the Haslam 408 MHz map (Haslam et al.

⁸ Millisecond pulsars in the galactic halo may contribute to the haze signal at some level (see Malyshev et al. 2010), but their morphology would also likely be spherical instead of significantly elongated in latitude.

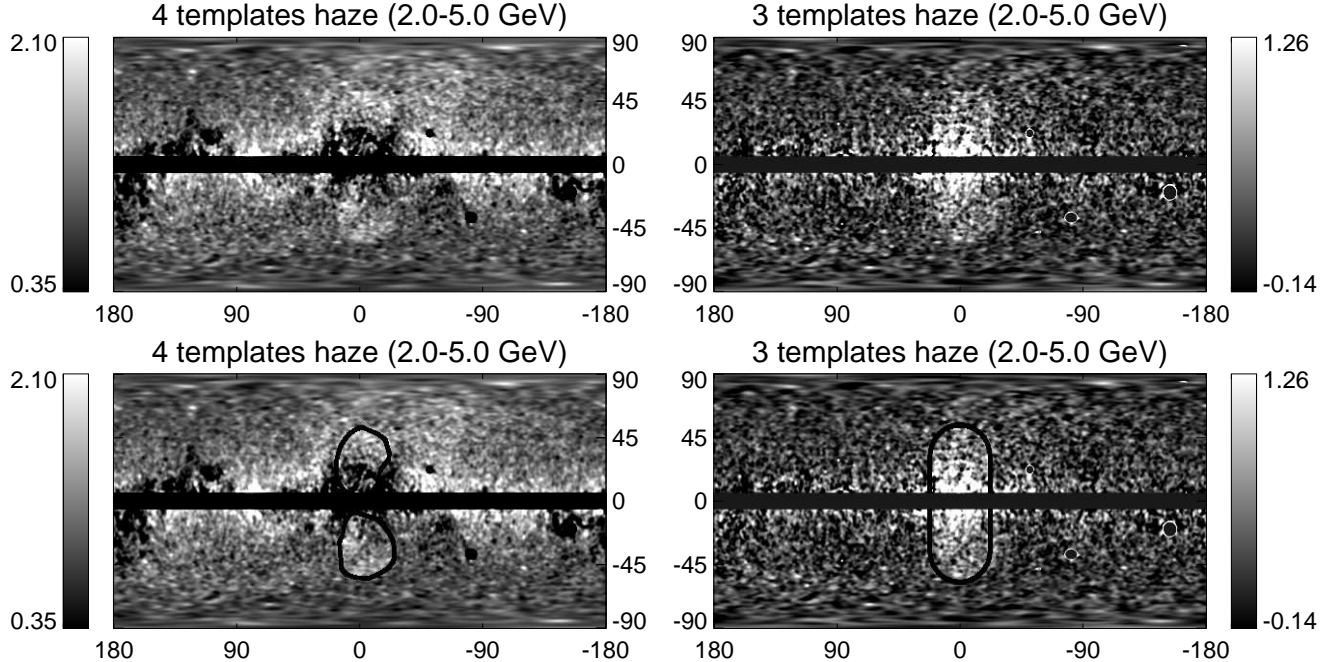


FIG. 1.— *Upper left:* The haze residual using the 4 templates fit (disk, SFD, uniform, bubble) defined in Su et al. (2010). The haze residual in this case is very pinched in the center and resembles two “bubbles”; however, note the significant regions of over-subtraction near the disk which pinch the haze towards the center. *Upper right:* The haze residual using the 3 templates fit ($E_{0.5}^{1.0}$, uniform, GALPROP). Although there is more noise, there is now very little disk over-subtraction and the haze looks much more like an “oval”. *Bottom row:* the same residuals with hand drawn contours over-plotted to highlight the morphological differences.

1982), and a bivariate Gaussian haze template were used. Method 2) was not particularly successful at fitting the full sky data and left significant disk-like residuals as well as the *Fermi* haze. Method 1) and 3) were much more successful but gave very different haze morphologies at low latitudes ($|b| < 30$ deg). In particular, using method 1) gives a haze which is more oval shaped while method 3) gives a haze which is more hourglass or “bubble” shaped (see Figure 1). Recently, Su et al. (2010) explored the bubble morphology of method 3) in detail and argued that this morphology may be indicative of a significant event towards the GC (e.g., accretion onto the central black hole) in the past. However, before ascribing a physical mechanism to the generation of the haze electrons which is dependent upon the haze morphology, it is important to determine what that morphology *is* and why the two methods differ.

Both methods 1) and 3) have associated problems. Since method 1) takes differences of *Fermi* data at different energies, any haze that is present in the lower energy data is subtracted off of the higher energy data so that the specific spectrum of the *Fermi* haze cannot be uniquely determined. In addition, since the *Fermi* maps have somewhat low signal to noise, subtracting one map from another (which adds the noise in weighted quadrature while removing the signal) yields difference maps that can be quite noisy.

On the other hand, method 1) has the advantage that it does not rely on external templates (like the SFD dust map for example) and so automatically takes into account systematics like line of density effects in the ISM. In other words, the lower energy *Fermi* maps are a better morphological tracer of the higher energy *Fermi* maps than external templates. The fact that the haze residual remains in the difference is a statement that this emission has a significantly harder spectrum than the emis-

sion elsewhere in the Galaxy.

The advantage of method 3) is that the absolute spectrum of the haze can be well determined since the haze structure is not in the external templates. However, because of line of sight variations in the ISM and cosmic-ray proton density, there will be, for example, variations in the ratio of π^0 gamma-ray emissivity to total dust column density. Thus the dust column map will not be a perfect tracer of the gamma-ray map. This is especially true in the inner Galaxy (within about 30 deg of the GC) and has the potential to significantly effect the perceived haze morphology. To illustrate this point, Figure 2 shows the *Fermi* data from 2.0-5.0 GeV with the Su et al. (2010) model for IC emission and varying amounts of the SFD map subtracted. When the SFD coefficient is small, the π^0 gammas are clearly under-subtracted. However, as the coefficient is increased, a clear “X” shaped over-subtraction becomes visible. This structure defines the “bubble” shape of the haze in method 3), and may be the root of the discrepancy between the two morphologies. That is, if the haze were actually oval shaped, it may appear more hourglass shaped after over-subtracting this “X”.

It is important to note that this “X” is not a feature *in* the SFD map (with the exception of the upper-right and possibly lower-right edges) but rather is being over-subtracted because the projected π^0 to dust column ratio is lower in that shape.

Furthermore, it is quite possible that the environmental conditions towards the GC which give rise to this “X” in gammas, produce similar features in X-rays and microwaves. For example, a heating source towards the center could heat the gas leading to enhanced, harder x-ray emission and such a variation in the environment would affect the estimate of column density to spinning dust emissivity used by Dobler & Finkbeiner (2008a,b) and

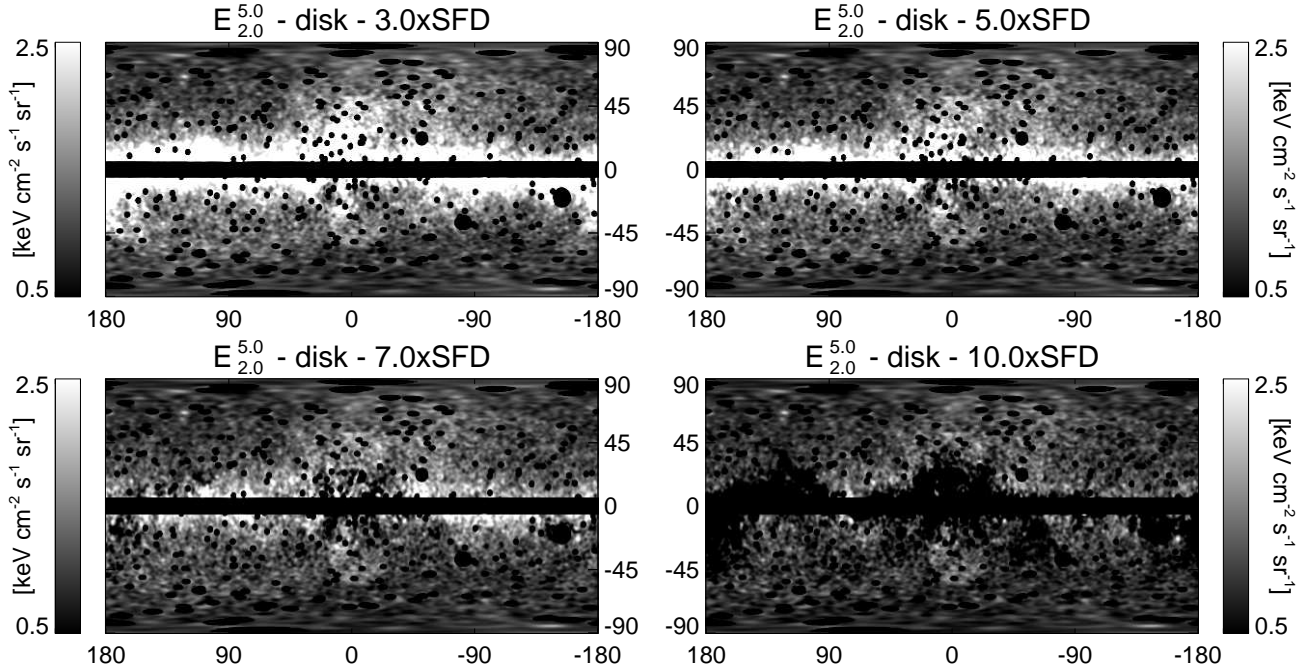


FIG. 2.— The *Fermi* data at 2.0-5.0 GeV minus the disk IC model of Su et al. (2010) plus varying amplitudes times the SFD dust map as a tracer of π^0 emission. As the SFD amplitude is increased a clear “X” shape or over-subtraction emerges towards the Galactic center. This is due to lower π^0 to dust column ratio in that shape towards the bulge likely caused by line of sight density variations of the ISM and cosmic ray protons. This X-shaped over-subtraction can make the oval shaped haze (right hand panel of Figure 1) appear more “bubble”-shaped (left hand panel of Figure 1).

Dobler et al. (2009) to remove the spinning dust component at microwaves. This would have the affect of making both the gamma-ray and microwave haze more hourglass shaped due to the same ISM physics which generates an edge in x-rays. Without speculating further what this “X” structure is, we note that there is significant evidence for X-shaped bulges in other galaxies, and recent evidence from the 2MASS survey that there exist red clump populations in the Milky Way that follow this feature (McWilliam & Zoccali 2010).

In the context of comparing the gamma-ray haze spectrum and morphology to a signal generated by injecting electrons via dark matter annihilations, the “bubble” morphology seems difficult to obtain (or at the very least, seems more indicative of a transient event in the GC). However, we show below that an oval shaped haze (and even an hourglass shaped haze) is possible with DM annihilation when considering anisotropic diffusion effects. Regardless, the underlying morphology of the gamma-ray haze at low latitudes is an unsettled issue. We choose to compare our results to the oval-shaped morphology and show that method 1) plus a dark matter contribution to the IC emission with anisotropic diffusion effects is consistent with the data.

3. DIFFUSION MODEL

Since the basis for any anisotropic diffusion scenario is that electrons travel along ordered field lines, our diffusion model must first assume a geometry for the ordered component of the Galactic magnetic field. From there, this magnetic field can be related to specific diffusion parameters which appear in the diffusion equation. All of our calculations are done by modifying the CR propagation code GALPROP (Strong & Moskalenko 1998, 2001; Moskalenko et al. 2003; Ptuskin et al. 2006; Strong et al. 2007) to include anisotropic effects.

3.1. Galactic magnetic field model

Our magnetic field model consists of two components: an irregular magnetic field B_{irr} and an ordered magnetic field B_{ord} . The former is parameterized as an exponential disk,

$$B_{\text{irr}} = B_0 e^{(R_\odot - r)/r_1 - |z|/z_1}, \quad (1)$$

where r and z are the radial and vertical distances from the GC respectively, and B_0 is the local value of the irregular component (i.e., at $r = R_\odot \approx 8.5$ kpc, the GC-sun distance). The ordered field is assumed to have the form,

$$B_{\text{ord}} = B_1 e^{-r/r_2 - |z|/z_2} \times \left(1 + K e^{-r/r_3 - |z|/z_3}\right), \quad (2)$$

where $B_1(1 + K)$ is the amplitude of the ordered field at the GC, which is based on the 3D field model of Orlando et al. (2010).

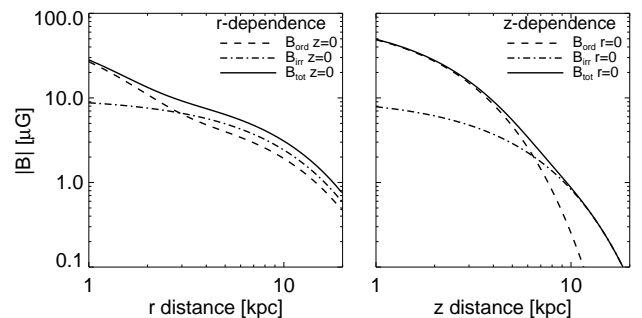


FIG. 3.— B-field amplitude profiles versus radial distance r (left) and versus distance above the galactic disk z (right).

The parameters B_0 , B_1 , K , $r_{1,2,3}$, and $z_{1,2,3}$ that we use are set by hand to reproduce the

TABLE 1

Model	B_{ord} Formula	B_0 (μG)	r_1 (kpc)	z_1 (kpc)	B_1 (μG)	K	r_2 (kpc)	z_2 (kpc)	r_3 (kpc)	z_3 (kpc)
1	$B_1 e^{-r/r_2 - z /z_2} \times (1 + K e^{-r/r_3 - z /z_3})$	3	7	4	8	10	7	2	0.8	10
2	$B_1 e^{-r/r_2 - z /z_2} \times \left(1 + K e^{-(r/r_3)^2} \sqrt{\cos(z /z_3 \times \pi/2)}\right)$	3	5	4	10	11	5	4	1	40
3	$B_1 e^{-r/r_2 - z /z_2} \times \left(1 + K e^{-(r/r_3)^{1.5} - z /z_3}\right)$	3	10	2	10	6	10	3	1.2	20
4	$B_1 e^{-r/r_2 - z /z_2} \times \left(1 + K e^{-(r/r_3)^{1.5} - (z /z_3)^{1.5}}\right)$	3.7	5	2	12.5	8	7	5	2.5	20
5	$B_1 e^{-r/r_2 - z /z_2} \times (1 + K e^{-r/r_3 - z /z_3})$	3.7	5	2	3.7	12	5	2	2	6

NOTE. — Magnetic field morphologies and parameters for the IC signals plotted in Figure 5. Our fiducial model is Model 1 which generates an IC signal that roughly matches the *Fermi* haze morphology (see Figure 6).

appropriate IC geometry and agree with measured values of the Galactic magnetic field at distances greater than ~ 1 kpc from the GC (Jansson et al. 2009; Sofue & Fujimoto 1983; Han & Qiao 1994; Beck 2001; Han 2002; Tinyakov & Tkachev 2002; Sun et al. 2008; Brown et al. 2007; Beck 2009; Jaffe et al. 2010; Nishiyama et al. 2010, see Figure 3). The parameters of our fiducial model (Model 1) are shown in Table 1. These give a local value for the total magnetic field of $5.4 \mu\text{G}$ and an ordered-to-total amplitude ratio of ≈ 0.62 which agrees well with measured values (see Beck 2009, and references therein).⁹

3.2. Anisotropic diffusion

The propagation of CRs through the ISM is governed by the diffusion equation,

$$\frac{\partial \psi}{\partial t} = \frac{\partial(b\psi)}{\partial E} + \vec{\nabla} \cdot (D \vec{\nabla} \psi) + Q, \quad (3)$$

where ψ is the number density per unit particle momentum of CRs at time t and position \vec{x} , b is an energy loss coefficient (dominated by synchrotron and IC in the case of electron CRs), Q is a source term due to the injection of electrons by DM annihilations, and D is the diffusion constant. It is this last parameter which must be modified for the case of anisotropic diffusion, and so we are concerned with the $\vec{\nabla} \cdot (D \vec{\nabla} \psi)$ term above.

We solve Equation 3 using GALPROP on a cylindrical grid so that,

$$\vec{\nabla} \cdot (D \vec{\nabla} \psi) = \frac{1}{r} \frac{\partial}{\partial r} (r D \frac{\partial \psi}{\partial r}) + \frac{\partial}{\partial z} (D \frac{\partial \psi}{\partial z}). \quad (4)$$

Typically, isotropic diffusion is assumed so that D is not a function of $\vec{x} = (r, z)$. However in our case Eq. 4 generalizes to:

$$\begin{aligned} \vec{\nabla} \cdot (D \vec{\nabla} \psi) = & \frac{1}{r} \frac{\partial}{\partial r} (r D_{rr} \frac{\partial \psi}{\partial r} + r D_{rz} \frac{\partial \psi}{\partial z}) \\ & + \frac{\partial}{\partial z} (D_{zz} \frac{\partial \psi}{\partial z} + D_{zr} \frac{\partial \psi}{\partial r}), \end{aligned} \quad (5)$$

⁹ These parameters do give a somewhat high value of $89 \mu\text{G}$ for the total field at the very center, $r = z = 0$ kpc. However, we note that not only is this in agreement with the estimates of Crocker et al. (2010) who place a *lower* limit of $50 \mu\text{G}$ in the inner 400pc from necessary synchrotron cooling to avoid violating existing diffuse γ -ray bounds, but also the very center is well outside our region of interest. Our mask of the Galactic plane extends up to $|b| = 5$ deg or $|z| \approx 0.75$ kpc. Inside this region, our choice of B-field has little impact on our results and our value at the center is only due to our specific parameterization of the field which likely does not extend in to arbitrarily small distances.

where D_{rr} , D_{zz} , D_{rz} and D_{zr} are functions of $\vec{x} = (r, z)$. For details of the implementation of this anisotropy in the GALPROP code, see Appendix A.

All that remains is to relate the diffusion tensor coefficients D_{rr} , D_{zz} and $D_{rz} = D_{zr}$ to the magnetic field model. Parker (1965) describes the propagation of particles along ordered field lines in the presence of an irregular component, and in this case, the diffusion tensor can be written,

$$D_{ij} = D_0 \left(\frac{\nu^2 \delta_{ij} + \Omega_i \Omega_j}{\nu^2 + \Omega^2} \right), \quad (6)$$

where D_0 is the diffusion constant for the isotropic case, δ_{ij} is the delta function, Ω_i is the cyclotron frequency due to the field pointed along the i -direction ($\Omega_i \propto B_i$ and $\Omega^2 = \Omega_i^2 + \Omega_j^2$), and ν is the characteristic frequency of deflections by the irregular component ($\nu \propto B_{\text{irr}}$). In our case, we assume for simplicity that the ordered field is oriented perpendicular to the Galactic plane, $B_r = 0$ and $B_z = B_{\text{ord}}$, so that $D_{rz} = D_{zr} = 0$. In this case, the diffusion tensor becomes,

$$D_{ij} = D_0 \times \begin{pmatrix} (1 + B_{\text{rat}}^2)^{-1} & 0 \\ 0 & 1 \end{pmatrix}, \quad (7)$$

where B_{rat} is the ratio of the ordered to irregular field and we have used the fact that $\Omega/\nu \propto B_{\text{ord}}/B_{\text{irr}}$. Note that, in the limit of $B_{\text{ord}} \rightarrow 0$, $D_{rr} = D_{zz} = D_0$, and in the limit of $B_{\text{irr}} \rightarrow 0$, $D_{rr} \rightarrow 0$ as desired. The form of this diffusion tensor implies that adding an ordered field suppresses diffusion perpendicular to that field.

For the diffusion tensor *coefficient*, we assume $D_0 \propto E^{-0.43}$. However, in contrast to most studies involving GALPROP, we incorporate the dependence of D_0 on B_{tot} as well. In particular following Strong et al. (2007),

$$D_0 \propto \left(\frac{B_{\text{irr}}}{B_{\text{tot}}} \right)^{-2} \times r_{\text{gy}} = \frac{B_{\text{tot}}}{B_{\text{irr}}^2}, \quad (8)$$

and because B depends on position, $D_0 = D_0(r, z)$. We set the normalization to be the locally measured value at roughly the locally measured magnetic field amplitude if the field were completely irregular, so that our final diffusion coefficient can be written as,

$$D_0 = 2.0 \times 10^{28} \text{ cm}^2/\text{s} \left(\frac{5 \mu\text{G}}{B_{\text{irr}}/B_{\text{tot}}} \right) \left(\frac{E}{4.0 \text{ GeV}} \right)^{-0.5}, \quad (9)$$

where the normalization is fixed by fitting to the local CR measurements.

Taken together, Equations 7 and 9 completely define our anisotropic diffusion model and reduce to the

isotropic case when $B_{\text{ord}} \rightarrow 0$ and $B_{\text{irr}} \rightarrow \text{constant}$. For more details about the dependence of diffusion on the magnetic field, see Appendix B.

Lastly we note that, in all of our models, we use a box height $L_{\text{box}} = \pm 20$ kpc. This is not directly comparable to the usual box heights (~ 4 kpc) discussed in the literature, because the “free escape” of electrons outside the Galactic disk is taken into account by the spatial dependence of the diffusion tensor. This is in agreement with findings by the *Fermi* team regarding diffuse IC away from the GC (Porter 2010) and is in fact a more appropriate box size. This also alleviates the problem of “squashed” morphologies that are typical of smaller box heights when the CR density at the boundary is set to zero.

3.3. DM annihilation model

In Equation 3, the source term Q is the rate of e^+e^- injection by DM annihilations and is given by

$$Q(r, z) = \frac{1}{2} \langle \sigma v \rangle \frac{dN}{dE} \left(\frac{\rho(r, z)}{M_\chi} \right)^2, \quad (10)$$

where dN/dE is the injection spectrum and ρ is the Galactic DM halo. We assume a prolate Einasto (Einasto 1965) halo,

$$\rho(r, z) \propto \exp \left[-\frac{2}{\alpha} \left(\left(\frac{r^2}{r_c^2} + \frac{z^2}{z_c^2} \right)^{\alpha/2} - \frac{R_\odot^\alpha}{r_c^\alpha} \right) \right], \quad (11)$$

with $z_c/r_c = 2.0$, $z_c = 27$ kpc, and $\alpha = 0.17$ (Merritt et al. 2005). The overall normalization is set so that the local DM density is $\rho(R_\odot, 0) = 0.4$ GeV/cm³ (Catena & Ullio 2010).

The injection spectrum dN/dE is governed by the specific particle model. In our case, we use XDM (Finkbeiner & Weiner 2007) as our fiducial model, with $M_\chi = 1.2$ TeV, an annihilation channel $\chi\chi \rightarrow \phi\phi$, $\phi \rightarrow e^+e^-$, and with branching ratio 1 (hereafter, XDM e^\pm ; see Cholis et al. 2009c,b). In this model, ϕ is a vector boson with $m_\phi \leq 2m_\mu$ that is the force carrier responsible for the velocity dependent Sommerfeld enhancement (Arkani-Hamed et al. 2009; Pospelov & Ritz 2009). We do not include specific dynamics for the host halo, but we do assume that the velocity dispersion (and hence the Sommerfeld enhancement or “boost factor”) as well as substructure contribution is flat with radius. We define this boost factor BF as,

$$BF = \frac{\langle \sigma v \rangle}{3 \times 10^{-26} \text{ cm}^3/\text{s}}. \quad (12)$$

This model for the DM particle has $E^2 dN/dE \propto E^2$ as required by the CR, microwave, and gamma-ray data (Lin et al. 2010).

3.4. Fitting Procedure

We follow a similar procedure as that outlined in Appendix C of Dobler et al. (2010). Specifically, we generate a synthetic sky map,

$$S(E) = A_{\text{IoE}} \times E_{0.5}^{1.0} + A_{\text{gp}} \times G(E) + U(E), \quad (13)$$

where A_{IoE} and A_{gp} are the amplitudes of the *Fermi* 0.5-1.0 GeV map and the GALPROP map at mean

energy $E = \sqrt{E_0 E_1}$ respectively and $U(E)$ is a uniform background, and convert to a synthetic counts map $\mu(E) = S(E) \times (\text{mask}) \times (\text{exposure})$. We then minimize the log-likelihood,

$$\ln \mathcal{L} = \sum_i [k_i \ln \mu_i - \mu_i - \ln(k_i!)], \quad (14)$$

where k_i is the map of observed counts at pixel i , over the parameters A_{IoE} and A_{gp} . When comparing maps at different energies, it is important to smooth the templates and data to a common beam full-width half-maximum (FWHM). All of our maps use 1.6 years of data, are smoothed to 2 degrees, and for the $E_{0.5}^{1.0}$ map, we use only “front” converting events (see Dobler et al. 2010).

4. RESULTS

Figure 4 shows the GALPROP IC map for $E = 3.0$ GeV and for various assumptions about the dark halo prolateness and anisotropic diffusion. For the case of a spherical halo with isotropic diffusion (completely tangled magnetic field), the resultant IC signal is largely spherical. The same is true for our anisotropic model with a spherical halo, implying that diffusion effects alone cannot create the observed morphology. In fact prolate halos lead to IC morphologies which very closely resemble the haze morphology. In detail, we find that the prolate halo with isotropic diffusion is overly concentrated towards the center and that the best morphological match to the data comes from using a prolate halo with anisotropic diffusion.

The detailed assumptions on the B-field morphology, and thus on the spatial dependence of the diffusion, can have a strong effect on the observed morphology of the IC emission as is shown in Figure 5 where we present the IC maps at 3 GeV for four distinctively different B_{ord} assumptions from those of Equation 2. The specific magnetic field model can lead to various IC morphologies from more uniform to more centrally concentrated and from more elliptical to more circular. In addition, for fields with a strong ordered component towards $r = 0$ kpc, forked morphologies (due to increased synchrotron losses towards $r = 0$ kpc) are found. Interestingly, for relatively modest changes to our magnetic field parameters, we can also reproduce an *hourglass* shape reminiscent of the “bubble” shape in Su et al. (2010). Note that all models use an identical prolate dark matter halo; the variations in shape are due exclusively to magnetic field effects on the diffusion and relative energy losses to synchrotron and IC.

This IC emission is the combination of electrons scattering CMB, IR, and starlight photons. Each of these ISRF components has a distinct morphology, and so the IC emission from each will also have a different morphology. In fact, since the starlight and IR photons are mostly confined to the plane, the high latitude IC emission is due primarily to scattering of CMB photons. This is borne out in Figure 6 which shows the morphology of each of the IC components. The starlight and IR IC photons are concentrated much more towards the GC while the CMB IC photons extend to much higher latitudes. Furthermore, it is interesting to note the distinct “bubble”-like morphology of the CMB component. The implication here is that template fits like those used in Dobler et al. (2010) and Su et al. (2010), which use external templates that are concentrated towards the GC

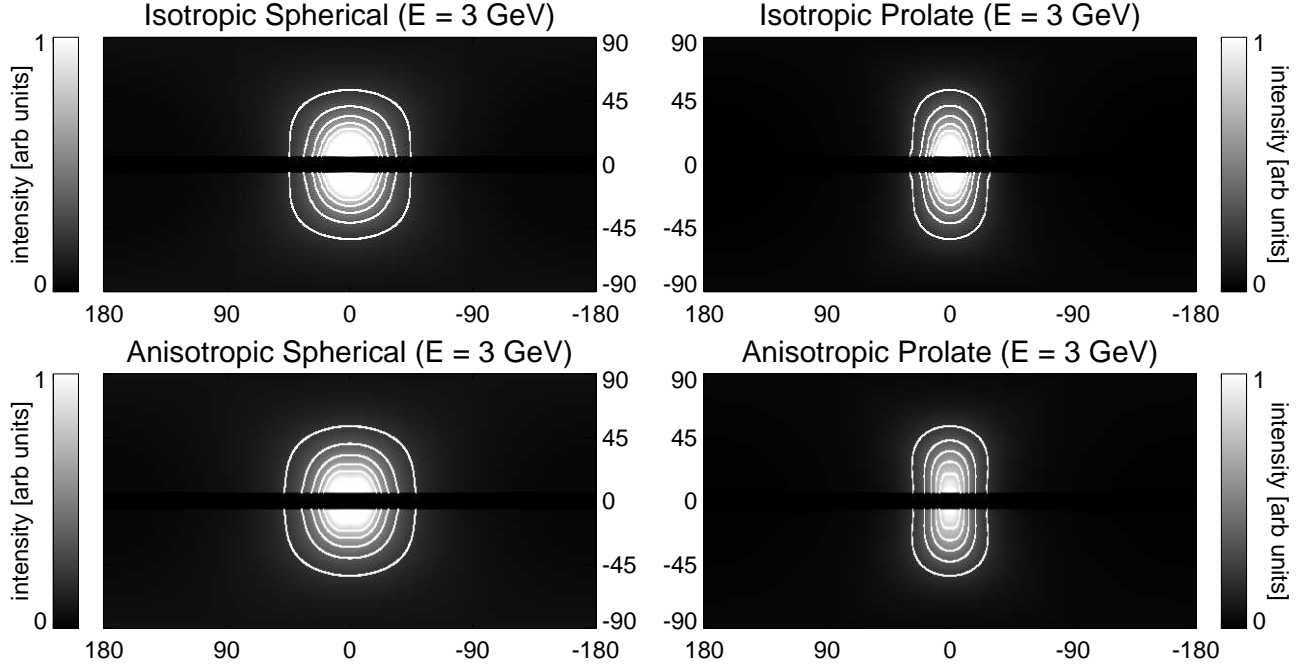


FIG. 4.— GALPROP IC at 3 GeV due to e^\pm production by DM annihilations with different assumptions about the halo shape and diffusion model: a spherical Einasto halo with isotropic diffusion (*upper left*), an axis ratio 2 prolate halo with isotropic diffusion (*upper right*), a spherical halo with anisotropic diffusion effects (*lower left*), and a prolate halo with anisotropic diffusion effects (*lower right*). All plots are arbitrarily normalized to the same intensity at $(\ell, b) = (0, 50)$ degrees. The spherical halos are clearly inconsistent with the haze morphology (see the right hand panels of Figure 1) while the prolate halos provide a significantly improved fit. In particular, the anisotropic diffusion case gives a morphology that has both the observed axis ratio and concentration.

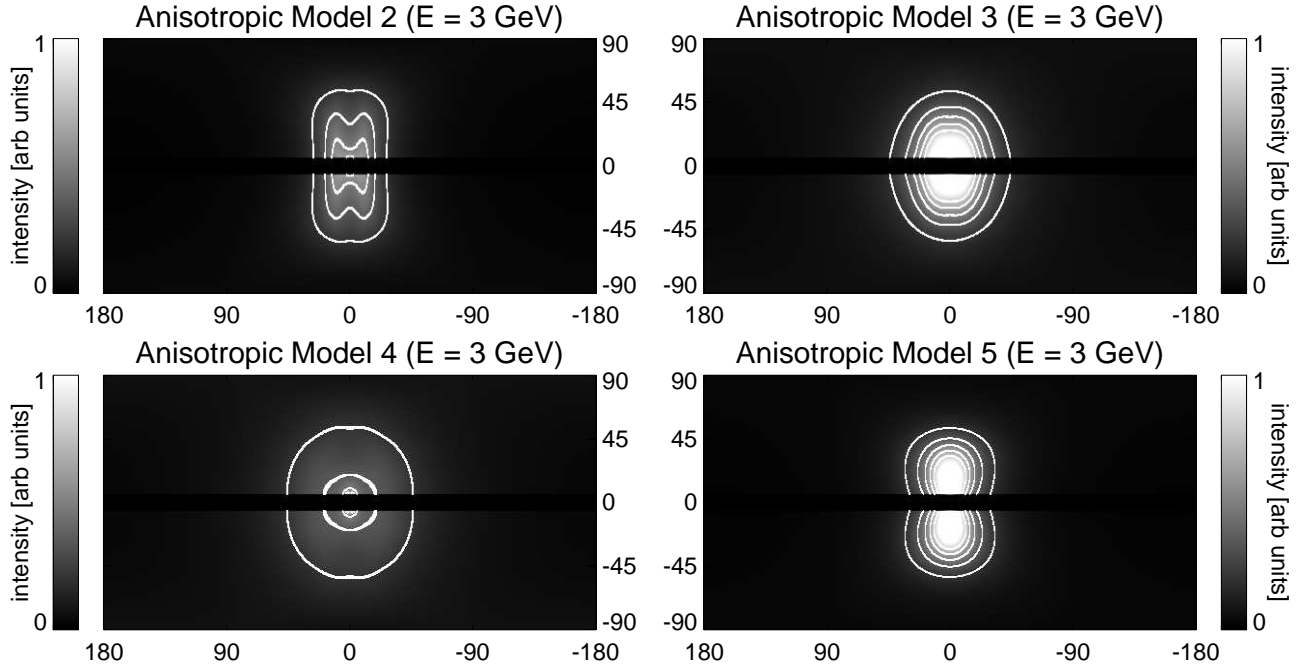


FIG. 5.— The same as the bottom right panel of Figure 4 but for several different models of the ordered magnetic field (see Table 1). Different magnetic field models can lead to various IC morphologies including forked (*top left*, due to increased synchrotron losses towards $r = 0$ kpc), circular and centrally concentrated (*top right*), circular and more uniform (*lower left*), and also more hourglass-shaped (*lower right*). See §4 for a description.

could potentially absorb the starlight and IR morphologies, while leaving the CMB morphology which appears more bubble-like. That is, if the intrinsic haze morphology is more oval-shaped, pulling out only the CMB component would may leave a bubble morphology.

In Figure 7 we show the residual “haze” map,

$$\mathcal{H}_{E_0}^{E_1} = E_{E_0}^{E_1} - S_{E_0}^{E_1} + A_{\text{gp}} \times G(E), \quad (15)$$

as well as the residual map,

$$\mathcal{R}_{E_0}^{E_1} = E_{E_0}^{E_1} - S_{E_0}^{E_1}. \quad (16)$$

As shown in the figure, the three component model provides a remarkably good fit to the data. There is some

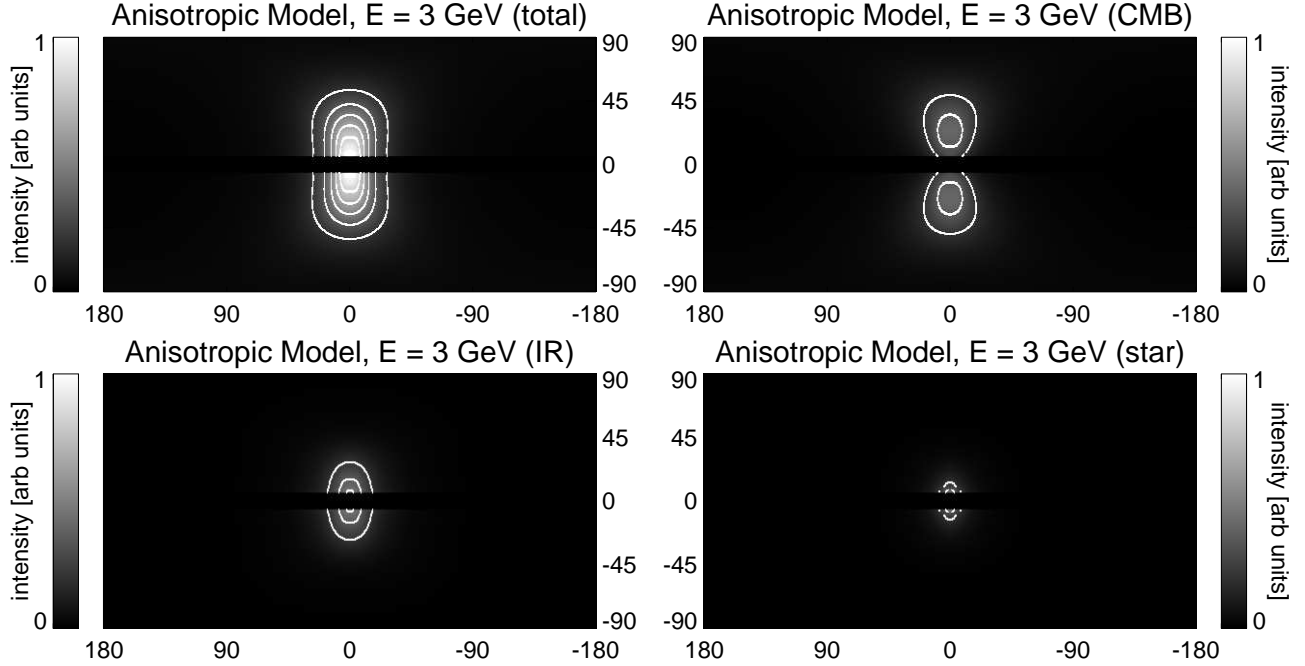


FIG. 6.— The full anisotropic, prolate model at 3 GeV (*top left*) as well its individual components broken down into photons from IC scattered CMB (*top right*), IR (*bottom left*), and starlight (*lower right*) photons. All maps use the same stretch, normalization, and contour intervals. The CMB component in particular has a distinctly “bubble”-like morphology. Thus, when using template regression techniques to assess the underlying morphology of the haze, care must be taken not to regress out emission from IR and starlight components while leaving only the CMB component.

residual over-subtraction due to the fact that the *Fermi* haze appears to have an “edge” at roughly $|b| \sim 50$ deg. This feature cannot be reproduced exactly by our models which tend to be slightly more diffuse. This lack of an edge pushes the fit to slightly over subtract the GALPROP haze contribution. Indeed, astrophysical models such as winds (Crocker et al. 2011) or jets would also either not have an edge or, in the case of jets, likely have a shock heated edge with a harder spectrum which is not clearly seen in the data (Su et al. 2010). Despite this, our fit removes 96%, 89%, and 69% of the variance over pixels with $|b| > 5^\circ$ at $E = 2\text{-}5$, $5\text{-}10$, and $10\text{-}20$ GeV respectively (see Figure 7).

Lastly, we compare the spectrum of the observed *Fermi* haze to that produced by the IC emission from e^\pm generated by the XDM electrons annihilation channel. We plot the $\mathcal{H}(E)$ emission in the window defined by $|\ell| < 20$ deg and $10 < |b| < 50$ deg. This region is dominated by the *Fermi* haze and is relatively free of other foregrounds. When comparing the spectra, it is important to keep in mind that $\mathcal{H}(E)$ has the *Fermi* $E_{0.5}^{1.0}$ map times $A_{\text{loE}}(E)$ removed, and so in Figure 8 we show the intensity versus E for $\mathcal{H}(E)$ and $G(E) - A_{\text{loE}}(E) \times G_{0.5}^{1.0}$.

Performing an independent fit of the *Fermi* and WMAP haze profile (intensity as a function of latitude south of the GC) we find that the required BF for the *Fermi* haze at 4 GeV is $\text{BF}=24$ while at WMAP 23 GHz it is a nearly identical $\text{BF}=27$, as shown in the bottom panels of Figure 8. In our calculations of the synchrotron radiation emission, we take into account the presence of both the ordered and the irregular B-field components. In the upper right panel of Figure 8, the predicted DM spectrum is plotted over the *Fermi* data *assuming* a BF of ~ 24 . It is clear from the figure that the DM spectrum with this BF provides an excellent agreement with the data, especially taking into account uncertainties in the

optical and IR ISRF at latitudes far above the plane. While the cross section in the inner galaxy is roughly a factor of three lower than that needed to explain local cosmic ray excesses, this could naturally arise from a radius dependent velocity dispersion (Cholis & Weiner 2009), or from a depletion of substructure in the inner galaxy (Slatyer et al. 2011).

5. CONCLUSIONS

We have developed a model of Galactic cosmic-ray diffusion that incorporates both an ordered and turbulent magnetic field component. The ordered component results in anisotropic diffusion of cosmic-ray electrons along field lines. Combining this model of diffusion with dark matter annihilations in a prolate Galactic dark halo produces an inverse Compton gamma-ray signal that matches the morphology and spectrum of the observed *Fermi* gamma-ray haze. Namely, an oval-shaped haze with axis ratio ≈ 2.0 , extending up to $|b| \sim 50$ deg, and with a cosmic-ray injection spectrum $E^2 dN/dE \propto E^2$.

The detailed morphology of the haze at low latitudes is still uncertain. We have shown that the dust-column to π^0 gamma-ray ratio is higher in an “X” shaped morphology towards the center of the Galaxy and that using a map of dust column like the SFD dust map as a tracer of π^0 gammas results in an over-subtraction of the “X”. The end result is that an oval-shaped haze may then appear more “hourglass” or “bubble” shaped. Using the 0.5-1.0 GeV *Fermi* map itself (which contains very little of the gamma-ray haze) as a tracer of disk emission at higher energies is immune to these line of sight effects and produces a more oval-shaped haze at the cost of noisier residuals.

Regardless, a three component model of anisotropic diffusion with dark matter annihilations in a prolate halo plus the *Fermi* 0.5-1.0 GeV map plus a uniform back-

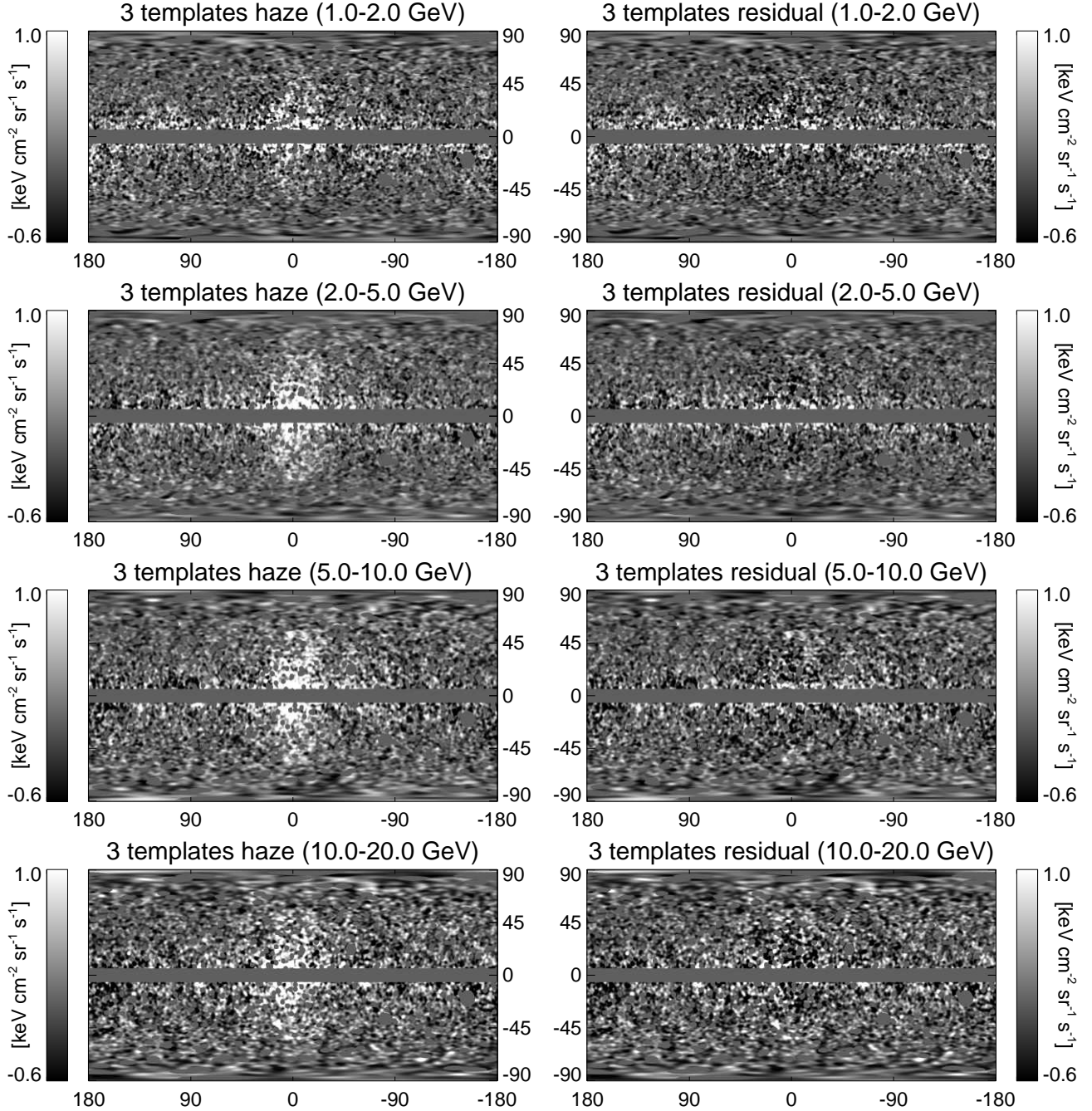


FIG. 7.— The haze (left column) and residuals (right column) of our three template fit in energy bins from 1.0 to 20.0 GeV. The haze maps clearly show the strong haze residual with an axis ratio ≈ 2 that is in reasonably good morphological agreement with our anisotropic dark matter model (see Figure 6 top left panel). This is borne out in the residual maps which show a residual consistent with noise at latitudes above 20° . Close inspection reveals a slight over-subtraction towards the center due to the fact that our model does not explicitly include an “edge” at $b \approx \pm 50^\circ$ as is seen in the data.

ground provides an excellent fit to the data from 1-20 GeV. The self-annihilation cross section required for the dark matter generated IC component is $\sim 9 \times 10^{-25} \text{ cm}^3/\text{s}$ (boost factor ~ 30), which is easily obtainable via the Sommerfeld enhancement in our models and also produces the microwave haze. Furthermore, this boost factor is well within the bounds of thermal relic and CMB constraints (Slatyer et al. 2009; Zavala et al. 2010).

The most significant outstanding issues are the sharp “edges” of the haze at high latitudes and also the morphology of the haze at low latitudes. Sharp edges are not particularly expected with either a dark matter annihila-

tion or astrophysical (such as winds or jets) mechanism, unless the spectrum at the edge is significantly hardened as does not appear to be the case. Magnetic confinement could potentially help both explanations, though care must be taken not to significantly synchrotron brighten the edges which are not seen in the WMAP microwave data. The low latitude morphology of the haze (“oval” versus “bubble” shape) may become more clear as more data are collected by *Fermi*. In particular, at high energies, the disk fades much more quickly than the haze because of the softer spectrum of the disk, and so the low latitude haze may be revealed at high energies with

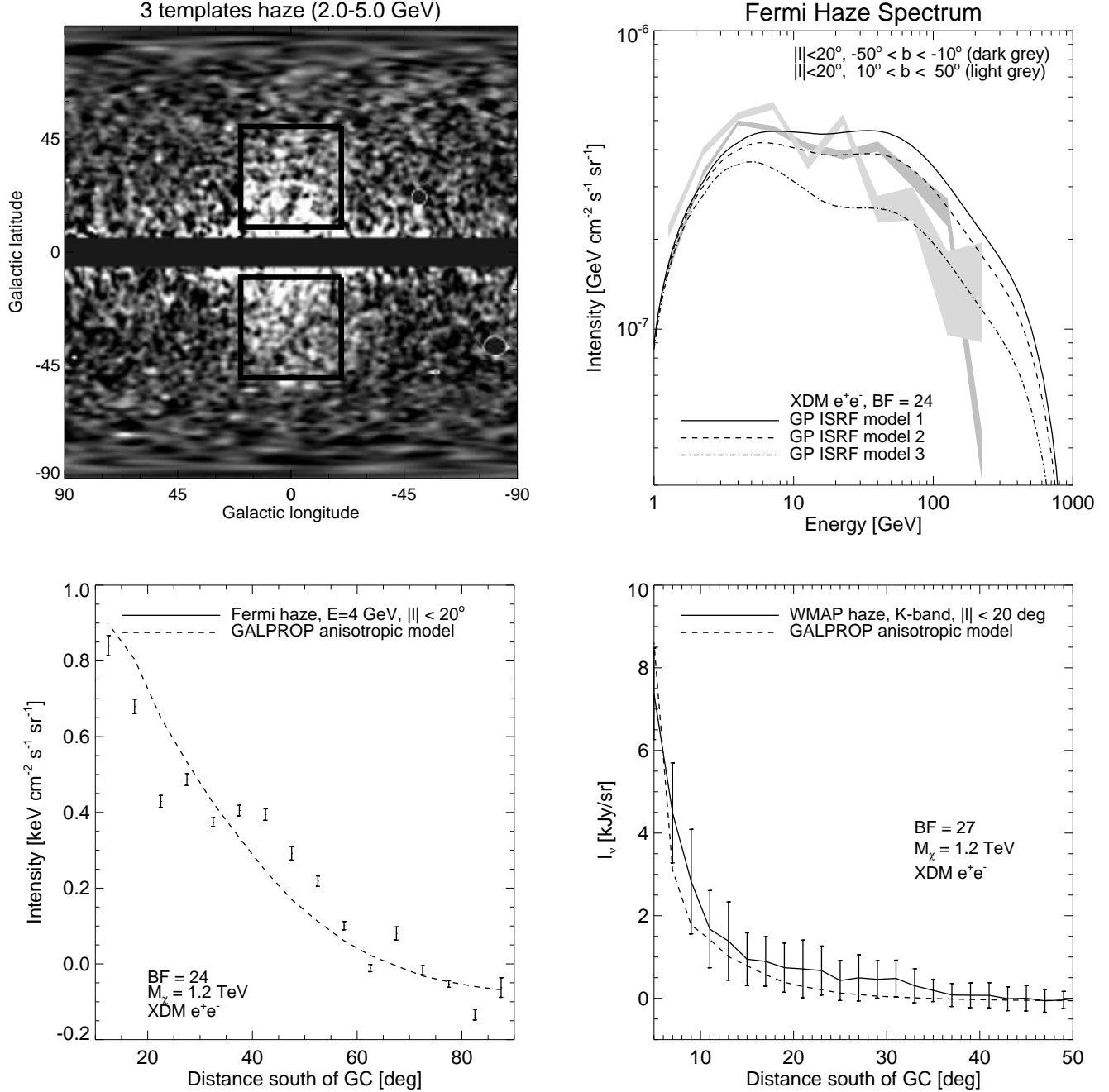


FIG. 8.— *Upper left*: A zoom in of the haze from Figure 1 with the two black boxes indicating the area used to plot the spectrum shown in the *upper right*. The light and dark bands represent the spectrum of emission in the north and south boxes respectively. The spectrum from DM annihilations (solid lines) is quite consistent with the data especially when taking into account uncertainties in the IR and starlight components of the ISRF at high latitudes. The dashed and dot-dashed lines are for the same model with varying IR and starlight intensities (20% and 50% reduction in IR and starlight intensities respectively). The required boost factor is nearly identical to that found by fitting the radial profile south of the GC to the *Fermi* 4 GeV data (*bottom left*) as well independently fitting the microwave haze profile at WMAP K-band (*bottom right*).

5 to 10 more years of data.

Of course, there is the possibility of a hybrid scenario in which some event evacuates a cavity towards the Galactic center that is filled with high energy electrons from dark matter annihilation that are trapped by magnetic confinement. Su et al. (2010) discount this possibility under the assumption that the dark matter signal would be more spherical, but we have shown here that this is not the case in general for triaxial halos. Injection from dark matter annihilation would also have the advantage that the hard spectrum can be obtained (as we have shown in

this paper) and the injection is *extended*. Nevertheless, inside the edge, the haze appears to have a profile that is roughly flat in latitude above $|b| > 30^\circ$. Such a projected profile seems nearly impossible to realize (either with astrophysical or dark matter models) unless electrons pile up on the edges, though the naive expectation would be that the gammas would be limb-brightened which is not observed. If these features persist in future data, such hybrid scenarios are inevitable.

Lastly, we point out that introducing a significant ordered field as we have could potentially produce a sig-

nificantly polarized microwave signal. By design, our model does reproduce the observed microwave haze in total temperature; comparison with the WMAP polarization data will be the subject of future work.

6. ACKNOWLEDGMENTS

The authors would like to thank Douglas Finkbeiner, Joseph Gelfand, and Ronnie Janson for helpful conversations. We especially thank Lisa Goodenough for provid-

ing valuable insights with respect to anisotropic propagation using GALPROP. GD is supported by the Harvey L. Karp Discovery Award. IC has been partially supported by DOE OJI grant # DE-FG02-06ER41417, and also by the Mark Leslie Graduate Assistantship. NW is supported by DOE OJI grant #DE-FG02-06ER41417 and NSF grant #0947827, as well as by the Ambrose Monell Foundation.

REFERENCES

- Abdo, A. A., et al. 2009a, *Science*, 325, 848
 —. 2009b, *ApJ*, 700, 597
 —. 2009c, *ApJ*, 703, 1249
 —. 2009d, *Physical Review Letters*, 102, 181101
 —. 2010a, *JCAP*, 4, 14
 —. 2010b, *ApJ*, 722, 520
 —. 2010c, *Physical Review Letters*, 104, 101101
 —. 2010d, *ApJ*, 715, 429
 —. 2010e, *ApJS*, 187, 460
 —. 2010f, *ApJ*, 716, 30
 Ackermann, M., et al. 2010a, *Phys. Rev. D*, 82, 092004
 —. 2010b, *ApJ*, 717, L71
 Adriani, O., et al. 2009, *Nature*, 458, 607
 —. 2010, *Astroparticle Physics*, 34, 1
 Arkani-Hamed, N., Finkbeiner, D. P., Slatyer, T. R., & Weiner, N. 2009, *Phys. Rev.*, D79, 015014
 Beck, R. 2001, *Space Sci. Rev.*, 99, 243
 Beck, R. 2009, in *IAU Symposium*, Vol. 259, IAU Symposium, 3–14
 Brown, J. C., et al. 2007, *Astrophys. J.*, 663, 258
 Catena, R., & Ullio, P. 2010, *JCAP*, 8, 4
 Cholis, I., Dobler, G., Finkbeiner, D. P., Goodenough, L., & Weiner, N. 2009a, *Phys.Rev.*, D80, 123518
 Cholis, I., Finkbeiner, D. P., Goodenough, L., & Weiner, N. 2009b, *JCAP*, 0912, 007
 Cholis, I., Goodenough, L., & Weiner, N. 2009c, *Phys.Rev.*, D79, 123505
 Cholis, I., & Weiner, N. 2009, *arXiv:0911.4954*
 Cirelli, M., Franceschini, R., & Strumia, A. 2008, *Nucl. Phys.*, B800, 204
 Crocker, R. M., Jones, D. I., Aharonian, F., Law, C. J., Melia, F., & Ott, J. 2011, *MNRAS*, 411, L11
 Crocker, R. M., Jones, D. I., Melia, F., Ott, J., & Protheroe, R. J. 2010, *Nature*, 463, 65
 Diemand, J., Kuhlen, M., Madau, P., Zemp, M., Moore, B., Potter, D., & Stadel, J. 2008, *Nature*, 454, 735
 Dobler, G., Draine, B., & Finkbeiner, D. P. 2009, *ApJ*, 699, 1374
 Dobler, G., & Finkbeiner, D. P. 2008a, *ApJ*, 680, 1222
 —. 2008b, *ApJ*, 680, 1235
 Dobler, G., Finkbeiner, D. P., Cholis, I., Slatyer, T., & Weiner, N. 2010, *ApJ*, 717, 825
 Einasto, J. 1965, *Trudy Inst. Astrofiz. Alma-Ata*, 51, 87
 Faucher-Giguere, C. A., & Loeb, A. 2010, *JCAP*, 1001, 005
 Feng, J. L., Kaplinghat, M., & Yu, H.-B. 2010, *Phys. Rev.*, D82, 083525
 Finkbeiner, D. P. 2004a, *Astrophys. J.*, 614, 186
 —. 2004b, *arXiv:0409027*
 Finkbeiner, D. P., Goodenough, L., Slatyer, T. R., Vogelsberger, M., & Weiner, N. 2010
 Finkbeiner, D. P., & Weiner, N. 2007, *Phys. Rev.*, D76, 083519
 Gebauer, I., & de Boer, W. 2009, *arXiv:0910.2027*
 Han, J. 2002, *Astrophysical Polarized Backgrounds*, 609, 96
 Han, J. L., & Qiao, G. J. 1994, *A&A*, 288, 759
 Haslam, C. G. T., Salter, C. J., Stoffel, H., & Wilson, W. E. 1982, *A&AS*, 47, 1
 Hisano, J., Matsumoto, S., & Nojiri, M. M. 2004, *Phys. Rev. Lett.*, 92, 031303
 Hisano, J., Matsumoto, S., Nojiri, M. M., & Saito, O. 2005, *Phys. Rev.*, D71, 063528
 Jaffe, T. R., Leahy, J. P., Banday, A. J., Leach, S. M., Lowe, S. R., & Wilkinson, A. 2010, *MNRAS*, 401, 1013
 Jansson, R., Farrar, G. R., Waelkens, A. H., & Ensslin, T. A. 2009, *JCAP*, 0907, 021
 Kuhlen, M., Diemand, J., Madau, P., & Zemp, M. 2008, *Journal of Physics Conference Series*, 125, 012008
 Lattanzi, M., & Silk, J. I. 2009, *Phys. Rev.*, D79, 083523
 Lin, T., Finkbeiner, D. P., & Dobler, G. 2010, *Phys. Rev. D*, 82, 023518
 Linden, T., & Profumo, S. 2010, *Astrophys. J.*, 714, L228
 Longair, M. S. 2002, *High Energy Astrophysics*, Volume 2, pp. 346–352 (Cambridge University Press)
 Malyshev, D., Cholis, I., & Gelfand, J. D. 2010, *ApJ*, 722, 1939
 McQuinn, M., & Zaldarriaga, M. 2010, *arXiv:1004.1189*
 McWilliam, A., & Zoccali, M. 2010, *ApJ*, 724, 1491
 Merritt, D., Navarro, J. F., Ludlow, A., & Jenkins, A. 2005, *Astrophys. J.*, 624, L85
 Mertsch, P., & Sarkar, S. 2010, *JCAP*, 10, 19
 Moskalenko, I. V., Strong, A. W., Mashnik, S. G., & Jones, F. C. 2003, in *International Cosmic Ray Conference*, Vol. 4, *International Cosmic Ray Conference*, 1917
 Nishiyama, S., et al. 2010, *ApJ*, 722, L23
 Orlando, E., Strong, A. W., Moskalenko, I. V., Porter, T. A., Johannesson, G., & Digel, S. W. 2010, in *Bulletin of the American Astronomical Society*, Vol. 42, *Bulletin of the American Astronomical Society*, 704
 Parker, E. N. 1965, *Planet. Space Sci.*, 13, 9
 Picozza, P., et al. 2007, *Astropart. Phys.*, 27, 296
 Porter, T. 2010, *Talk given at TeV Particle Astrophysics (TeVPA)*, July 19–23, 2010
 Porter, T. A., et al. 2009, *arXiv:0907.0294*
 Pospelov, M., & Ritz, A. 2009, *Phys. Lett.*, B671, 391
 Press, W. H., Teukolsky, S. A., Vetterling, W. T., & Flannery, B. P. 1992, *Numerical recipes in FORTRAN. The art of scientific computing*, ed. Press, W. H., Teukolsky, S. A., Vetterling, W. T., & Flannery, B. P.
 Ptuskin, V. S., Moskalenko, I. V., Jones, F. C., Strong, A. W., & Zirakashvili, V. N. 2006, *ApJ*, 642, 902
 Saz Parkinson, P. M., et al. 2010, *ApJ*, 725, 571
 Schlegel, D. J., Finkbeiner, D. P., & Davis, M. 1998, *ApJ*, 500, 525
 Slatyer, T. R., Padmanabhan, N., & Finkbeiner, D. P. 2009, *Phys.Rev.*, D80, 043526
 Slatyer, T. R., Toro, N., & Weiner, N. 2011, in preparation
 Sofue, Y., & Fujimoto, M. 1983, *ApJ*, 265, 722
 Sommerfeld, A. 1931, *Annalen der Physik*, 403, 257
 Springel, V., et al. 2008, *MNRAS*, 391, 1685
 Strong, A. W., & Moskalenko, I. V. 1998, *ApJ*, 509, 212
 —. 2001, *Advances in Space Research*, 27, 717
 Strong, A. W., Moskalenko, I. V., & Ptuskin, V. S. 2007, *Annual Review of Nuclear and Particle Science*, 57, 285
 Strong, A. W., Porter, T. A., Digel, S. W., Jóhannesson, G., Martin, P., Moskalenko, I. V., Murphy, E. J., & Orlando, E. 2010, *ApJ*, 722, L58
 Su, M., Slatyer, T. R., & Finkbeiner, D. P. 2010, *ApJ*, 724, 1044
 Sun, X. H., Reich, W., Waelkens, A., & Enßlin, T. A. 2008, *A&A*, 477, 573
 Tinyakov, P. G., & Tkachev, I. I. 2002, *Astropart. Phys.*, 18, 165
 Zavala, J., Vogelsberger, M., & White, S. D. 2010, *Phys.Rev.*, D81, 083502
 Zentner, A. R., Kravtsov, A. V., Gnedin, O. Y., & Klypin, A. A. 2005, *ApJ*, 629, 219
 Zhang, J., et al. 2009, *Phys. Rev.*, D80, 023007

APPENDIX

A. ANISOTROPIC DIFFUSION IN THE GALPROP CODE

In GALPROP, the diffusion equation is solved through the Crank-Nicholson implicit method (Strong et al. 2007; Press et al. 1992):

$$\frac{\partial \psi_i}{\partial t} = \frac{\psi_i^{t+\Delta t} - \psi_i^t}{\Delta t} = \frac{\alpha_1 \psi_{i-1}^{t+\Delta t} - \alpha_2 \psi_i^{t+\Delta t} + \alpha_3 \psi_{i+1}^{t+\Delta t}}{\Delta t} + Q_i, \quad (\text{A1})$$

where i is the index of position (r or z) or momentum and $\alpha_{1,2,3}/\Delta t$ are the Crank-Nicholson coefficients. In the case where D is homogeneous in space, these coefficients are:

$$\frac{\alpha_1}{\Delta t} = D \frac{2r_i - \Delta r}{2r_i(\Delta r)^2}, \quad \frac{\alpha_2}{\Delta t} = D \frac{2r_i}{r_i(\Delta r)^2}, \quad \frac{\alpha_3}{\Delta t} = D \frac{2r_i + \Delta r}{2r_i(\Delta r)^2}, \quad (\text{A2})$$

for diffusion along r and

$$\frac{\alpha_1}{\Delta t} = \frac{D}{(\Delta z)^2}, \quad \frac{\alpha_2}{\Delta t} = \frac{2D}{(\Delta z)^2}, \quad \frac{\alpha_3}{\Delta t} = \frac{D}{(\Delta z)^2} \quad (\text{A3})$$

for diffusion along z . With the new terms from anisotropic diffusion (see Eq. 5) the Crank-Nicholson coefficients become:

$$\frac{\alpha_1}{\Delta t} = D_{rr_i} \frac{2r_i - \Delta r}{2r_i(\Delta r)^2} - \frac{D_{rr_{i+1}} - D_{rr_{i-1}}}{4(\Delta r)^2}, \quad \frac{\alpha_2}{\Delta t} = D_{rr_i} \frac{2r_i}{r_i(\Delta r)^2}, \quad \frac{\alpha_3}{\Delta t} = D_{rr_i} \frac{2r_i + \Delta r}{2r_i(\Delta r)^2} + \frac{D_{rr_{i+1}} - D_{rr_{i-1}}}{4(\Delta r)^2}, \quad (\text{A4})$$

for diffusion along r and

$$\frac{\alpha_1}{\Delta t} = \frac{D_{zz_i}}{(\Delta z)^2} - \frac{D_{zz_{i+1}} - D_{zz_{i-1}}}{4(\Delta z)^2}, \quad \frac{\alpha_2}{\Delta t} = \frac{2D_{zz_i}}{(\Delta z)^2}, \quad \frac{\alpha_3}{\Delta t} = \frac{D_{zz_i}}{(\Delta z)^2} + \frac{D_{zz_{i+1}} - D_{zz_{i-1}}}{4(\Delta z)^2}, \quad (\text{A5})$$

for diffusion along z , and where, as in the main text, we have taken $D_{rz} = D_{zr} = 0$ (since $B_r = 0$) for simplicity. When iterating recursively for a steady-state ψ , GALPROP utilizes the fact that the r and z directions are separable, whereas if we take $D_{rz} = D_{zr} \neq 0$, these directions are not separable. So while we use Eqs. A4 and A5 in practice, the general quantization of Eq. 5 is (superscripts are spatial indices for clarity)

$$\begin{aligned} \vec{\nabla}(D\vec{\nabla}\psi) = & \left(\frac{D_{rr}^{i,j}}{r^i} + \frac{D_{rr}^{i+1,j} - D_{rr}^{i-1,j}}{2\Delta r} + \frac{D_{rz}^{i,j+1} - D_{rz}^{i,j-1}}{2\Delta z} \right) \times \frac{\psi^{i+1,j} - \psi^{i-1,j}}{2\Delta r} + \\ & \left(\frac{D_{rz}^{i,j}}{r^i} + \frac{D_{rz}^{i+1,j} - D_{rz}^{i-1,j}}{2\Delta r} + \frac{D_{zz}^{i,j+1} - D_{zz}^{i,j-1}}{2\Delta z} \right) \times \frac{\psi^{i,j+1} - \psi^{i,j-1}}{2\Delta z} + \\ & D_{rr}^{i,j} \times \frac{\psi^{i+1,j} + \psi^{i-1,j} - 2\psi^{i,j}}{(\Delta r)^2} + D_{zz}^{i,j} \times \frac{\psi^{i,j+1} + \psi^{i,j-1} - 2\psi^{i,j}}{(\Delta z)^2} + \\ & D_{rz}^{i,j} \times \frac{\psi^{i+1,j+1} + \psi^{i-1,j-1} - \psi^{i+1,j-1} - \psi^{i-1,j+1}}{2\Delta r \Delta z}. \end{aligned} \quad (\text{A6})$$

B. DIFFUSION DEPENDENCE ON MAGNETIC FIELD

Let us consider the generic case of an electron traveling in a magnetic field with both an irregular B_{irr} and ordered B_{ord} component. As the electron spirals around the ordered field lines with cyclotron frequency Ω , there is a characteristic frequency ν at which the electron is scattered from its path by the irregular component. In the case of a strong ordered component $B_{\text{ord}} \gg B_{\text{irr}}$, $\Omega \gg \nu$ while for $B_{\text{ord}} \ll B_{\text{irr}}$, $\Omega \ll \nu$. In other words, for strong ordered fields, the electron spirals around the field line many times before it is deflected by the irregular component. As noted in §3.2, this behavior is written in the diffusion tensor as (Parker 1965):

$$D_{ij} = D_0 \left(\frac{\nu^2 \delta_{ij} + \Omega_i \Omega_j}{\nu^2 + \Omega^2} \right), \quad (\text{B1})$$

which, for the case of an ordered field completely along the z -direction, leads to the relation

$$\frac{D_{rr}}{D_{zz}} \propto \frac{1}{1 + B_{\text{ord}}^2/B_{\text{irr}}^2}. \quad (\text{B2})$$

We wish to motivate Equation B2 from the perspective of diffusion *lengths* λ since that is the most direct measure of the diffusion coefficient, $D_{ij} = \lambda_{ij}c/3$ (where c is the speed of light). In our scenario then,

$$\frac{\lambda_{zz}}{\lambda_{rr}} \sim \frac{r_{\text{gyr}} N}{r_{\text{gyr}}} \sim N, \quad (\text{B3})$$

where r_{gyr} is the gyroradius and N is the number of scatterings of the particle by angle $\phi \sim B_{\text{irr}}/B_{\text{tot}}$, which is the inclination angle of the field lines from the direction of the mean field due to irregularities (see Longair 2002). Note that, in the case of $B_{\text{irr}} \gg B_{\text{ord}}$, ϕ is large and particles are deflected significantly from their initial direction within

one gyroradius while for $B_{\text{irr}} \ll B_{\text{ord}}$, $\phi \ll 1$ and particles follow the field lines of the local ordered field. For the particle to scatter by ~ 1 radian, we need $\sqrt{N}\phi \sim 1$ which implies

$$\frac{\lambda_{zz}}{\lambda_{rr}} \sim \phi^{-2} \sim B_{\text{tot}}^2 / B_{\text{irr}}^2, \quad (\text{B4})$$

and since $B_{\text{tot}} = \sqrt{B_{\text{ord}}^2 + B_{\text{irr}}^2}$,

$$\frac{\lambda_{zz}}{\lambda_{rr}} \sim \phi^{-2} \sim (1 + B_{\text{ord}}^2 / B_{\text{irr}}^2) \quad (\text{B5})$$

as desired.

C. LOW FREQUENCY RADIO EMISSION

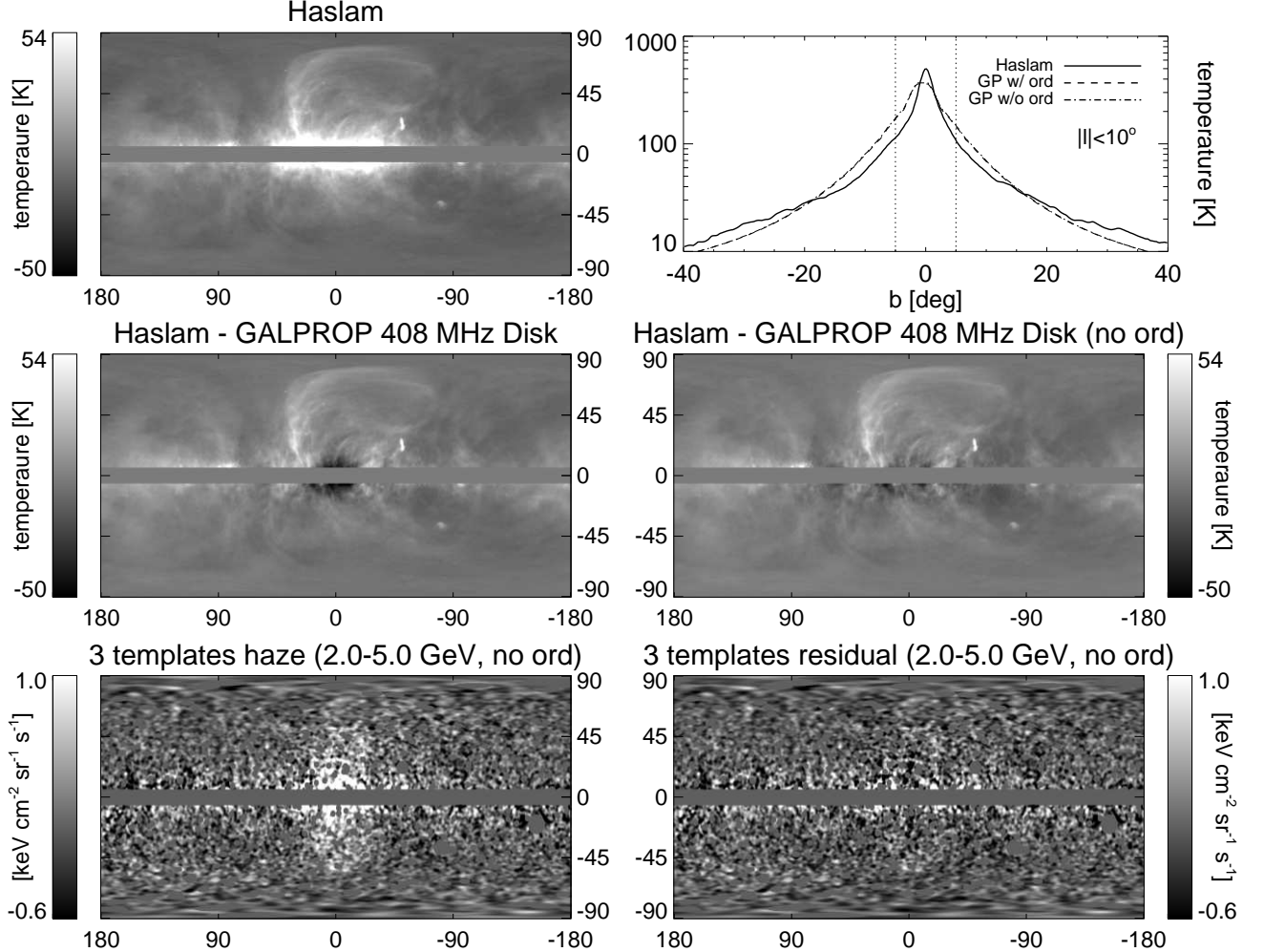


FIG. 9.— *Upper left*: The full sky Haslam 408 MHz map. *Upper right*: the latitudinal profile of Haslam and our 408 MHz synchrotron GALPROP map for primary electrons injected via SN shocks using our anisotropic diffusion model (both with and without the ordered field component). *Middle left*: Haslam minus our 408 MHz GALPROP map. While the agreement is in general quite good, the map is slightly too concentrated towards the center. This is alleviated by removing the ordered field (*middle right*) indicating that more complex ordered field morphologies than our simple parameterization allows can provide a good fit to the data. In addition to being a good fit to Haslam, the model without an ordered field is a reasonable match to the *Fermi* haze, though it is a bit centrally concentrated (*bottom panels*).

Dominated by synchrotron emission from electrons with energies \sim few GeV, the Haslam 408 MHz map (Haslam et al. 1982) provides an excellent constraint on both the injection morphology of the primary electrons via SN shock acceleration and also the magnetic field morphology. Thus, it is important to check that our anisotropic diffusion model maintains the “disk-like” shape of synchrotron from primary electrons at 408 MHz. Figure 9 shows the Haslam map, and the Haslam map and the predicted 408 MHz synchrotron emission due to SN injection using our full anisotropic model. As in Lin et al. (2010), we normalize the model to Haslam by setting the total emission in the region $|\ell| \leq 10^\circ$ and $-90^\circ \leq b \leq -5^\circ$ equal.

As shown in the radial profile panel (upper right), the agreement is very good, though the map difference (middle left panel) indicates that the stronger magnetic field in the center (due to the ordered component) may make the emission

somewhat steeper in the region $\sim 1\text{-}2$ kpc. However, we point out that, not only is the gamma-ray signal dominated by emission at higher latitudes, but we have used a very simple parameterization for the ordered field and additional field parameters (to lower the field within the inner 2 kpc) can remove the discrepancy. In fact, we can remove the ordered component altogether and the model comes into close agreement with both Haslam (middle right panel) and the *Fermi* data (bottom panels; also cf. Figure 4).